Earthshine and the Earth's Albedo II: Observations and Simulations Over Three Years

P.R. Goode, E. Pallé, V. Yurchyshyn, J. Qiu, J. Hickey, P. Montañés Rodriguez

Big Bear Solar Observatory, New Jersey Institute of Technology, Newark, NJ 07102, USA

M-C Chu

Department of Physics, The Chinese University of Hong Kong, Shatin N.T., Hong Kong

E. Kolbe

Department für Physik and Astronomie, Universität Basel, Basel, Switzerland

C.T. Brown, S.E. Koonin

W.K. Kellogs Radiation Laboratory, California Institute of Technology, Pasadena, CA 91125, USA

Abstract.

Since late 1998, we have been making sustained measurements of the earth's reflectance by observing the earthshine from Big Bear Solar Observatory. Further, we have simulated the earth's reflectance – for both the parts of the earth in the earthshine and the whole earth. The simulations employ scene models of the earth from the Earth Radiation Budget Experiment, simulated snow/ice cover and near real-time satellite cloud cover data. Broadly, the simulations and observations agree; however, there are important and significant differences, with the simulations showing more muted variations.

During the rising phase of the moon, we measure the sunlit world to the west of California, and during the declining lunar phase, we measure the sunlit world to the east. Somewhat surprisingly, the 1/3 of the earth to the west and that to the east have very similar reflectances, inspite of the fact that the topographies look quite different. The part to the west shows less stability, presumably because of the greater variability in the Asian cloud cover.

To determine a global albedo, we integrate over all lunar phases. Various methods are developed to perform this integration, and all give consistent results. Despite sizeable variation in the reflectance from night-to-night and season-to-season, which arises from changing cloud cover, we use the earthshine to determine annual albedos to better than 1%. As such, these measurements are significant for measuring climate variation and are an important complement to satellite determinations.

1. Introduction

In Qiu et al. (2003), hereafter Paper I, we have detailed our method of determining the earth's reflectance from photometric observations of the bright (moonshine) and dark (earthshine) parts of the lunar disk. We have demonstrated that we can measure the large-scale effective albedo of the earth to a precision of about 1% on any given night. Here we discuss the results of more than three years of observations of the earthshine. In addition, we have simulated the reflectance of the earth, treating separately the parts in the earthshine and all the sunlit earth throughout the hours of the day. In the simulations, we use scene models of the earth from the Earth Radiation Budget Experiment (ERBE) and near real-time satellite cloud cover data. We discuss and compare the observational results with those of the simulations.

On any one night, we determine the reflectance of most of the sunlit earth for a particular phase of the moon (the effective albedo). As detailed in Paper I, we need to integrate over all phases of the moon to determine a global or Bond albedo for the earth,

$$A = \frac{2}{3}\int_{-\pi}^{\pi} d\theta A^*(\theta) f_L(\theta)\sin\theta, \qquad (1)$$

where A^* is the effective albedo associated with a particular night, $f_L(\theta)$ is the moon's Lambert phase function and A is the Bond albedo.

As described in detail in Paper I, the effective albedo for an individual night is calculated from the earthshine measurements for that night using

$$A^*(\beta) = \frac{3}{2f_L}\frac{p_b f_b(\theta)}{p_a f_a(\theta_0)}\frac{I_a/T_a}{I_b/T_b}\frac{R_{em}^2}{R_e^2}\frac{R_{es}^2}{R_{ms}^2}, \qquad (2)$$

Paper number .
0148-0227/03/$9.00

where $\frac{I_a/T_a}{I_b/T_b}$ is the ratio of the earthshine intensity to the moonshine intensity in two opposing fiducial patches, after each is corrected for airmass, and $\frac{p_b}{p_a}$ is the ratio between the geometrical reflectivity of the two opposing fiducial patches. The lunar phase function for the bright side, $f_b(\theta)$, is used in the formula to account for the geometrical dependence of the reflectivity of the moon, while $f_a(\theta_0)$ accounts for the fact that the earthshine is not exactly retroflected from the moon ($\theta_0 \lesssim 1°$).

For convenience, the measured earth's albedo is often expressed as the magnitude of the effective albedo, A^*, i.e.,

$$[A^*] = -2.5 \log A^*. \tag{3}$$

This standard astronomical definition implies that the larger $[A^*]$ is the smaller the albedo. Note that a 1% change in A^* corresponds to about $0^m.01$ change in $[A^*]$.

Each night, we observe 10 fiducial patches, 5 on the Crisium side, and 5 on the Grimaldi side (see Figure 3 in Paper I). In principle, we obtain 25 values of A^* from the 25 combinations of the 5 pairs of fiducial patches. This gives us a way to evaluate the reliability of our measurement of A^* as detailed in section 5. Figure 10 (a) and (b) shows the A^* plot – morning (moon's phase angle decreasing toward new) and evening (moon's phase angle increasing toward full) – against lunar phase angle for the mean of the 25 datasets for each night. It is clear that the same pattern of variation appears in all datasets, indicating that this pattern is real, and not from measurement noise. We take an average of the 25 measurements of $[A^*]$ for each night as shown in Figure 10 (c), and the standard deviation of the mean in [A*] is calculated as 0.016 and 0.018 for morning and evening respectively, yielding a measurement accuracy of better than 2%. In detail, we calculated the $\sigma^2 = \frac{\Sigma_i([A^*]_i - \overline{[A^*]}_i)^2}{N-1}$, where N=5 and i=1-25.

So far, observational data have been accumulated for more than 40 months covering the winter of 1998-1999 through the early 2002 (1998 December 9 - 2002 March 31). We also have 73 nights of data from 1994 January 7 - 1995 August 4, which will be discussed in Paper III of this sequence (Pallé et al., 2003). Both the instantaneous $[A^*]$ variation during each single night, and the Bond albedo integrations over a long period of time, have been obtained and compared to the simulated results using a scene model, snow/ice cover data and satellite cloud cover data.

2. Modeling the Observations

In principle, we have sufficient information to determine a Bond albedo from the simulations by using scene models of the earth, and adding cloud cover data from satellites and snow/ice cover from models. However, a precise determination is no easy matter. In particular, the treatment of the clouds is probably a bit oversimplified, and we ignore any other climate parameters, beyond snow and ice, that might contribute to changes in albedo. Further, the ERBE model contemplates only 12 different scenes and 4 cloudiness levels (0-5%,5-50%, 50-95% and 95-100%). Beyond the appreciable binning of the cloud cover, changes in cloud type or cloud optical thickness, for example, will also affect the albedo, but these are not accounted for in the models. Thus, our albedo models presented here need to be considered only as a first order, or starting, approximation to the problem.

In general, the Bond albedo is given in terms of the albedo of each element of the earth's surface by,

$$A = \frac{1}{\pi R_e^2} \int d^2R (\hat{R} \cdot \hat{S}) a, \tag{4}$$

where d^2R is an element of the earth's surface, $\hat{R}$ is a unit vector pointing toward the local zenith, and $\hat{S}$ is a unit vector pointing toward the sun. The albedo of each surface element, a, depends on the surface type, cloud and snow/ice cover and solar zenith angle. The integral is over all portions of the globe illuminated by the sun (i.e.,$(\hat{R} \cdot \hat{S}) \geq 0$). However, to compare the simulations with our observations, we have to consider the ratio of the earthlight to sunlight, Γ, that would be seen by an observer on the moon.

There is a systematic variation of Γ throughout the lunar month. When the moon is nearly new (lunar phase $\theta \approx \pm\pi$), the earth is nearly full, and so Γ is relatively large ($\approx 10^{-4}$). Conversely, when the moon is nearly full ($\theta \approx 0$), the earth is a thin crescent and Γ becomes vanishingly small. Fluctuations of Γ about its systematic behavior are caused by varying terrestrial conditions, including weather, the seasons and climate change. The lunar phase θ is defined in Figure 2 of Paper I. After correction for the dependence of the reflectivity on lunar phase, one obtains

$$\Gamma = \frac{1}{\pi R_{em}^2} [\frac{R_{ms}}{R_{es}}]^2 \int_{(\hat{R}\cdot\hat{S}, \hat{R}\cdot\hat{M}) \geq 0} d^2R (\hat{R} \cdot \hat{S}) a (\hat{R} \cdot \hat{M}) L, \tag{5}$$

where $\hat{M}$ is the unit vector pointing from the earth toward the moon, and the integral is over all of the earth's surface for which the sun and moon are simultaneously above the horizon (i.e., $\hat{R} \cdot \hat{S}$ and $\hat{R} \cdot \hat{M} \geq 0$). The anisotropy function, L, generally depends on surface type, cloud cover, and the zenith angles and relative azimuth of the sun and moon. L is defined so that it is unity for a Lambert surface (see Equation (7) in Paper I). In terms of Equation (9) of Paper I,

$$A^* = \frac{3}{2 f_L} \Gamma \frac{R_{em}^2}{R_e^2} \frac{R_{es}^2}{R_{ms}^2}, \tag{6}$$

because Γ is the ratio of the earthshine to moonshine intensity that would be seen by an observer on earth looking at the moon, there is no dependence on lunar reflectivity.

Thus, our models enable us to simulate for a given night (or a subset of time during one night) the Bond albedo of the earth, and the effective albedo that would be seen from BBSO.

2.1. The Models

In modeling the reflectance properties, a and L, of the earth, we used scene models developed for the ERBE observations (Suttles et al., 1988). As mentioned, twelve scenes are tabulated, varying from "desert" (areas for which the annual precipitation is less than 26 cm) to "mixed land-ocean" areas, which are cells bordered by two land and two ocean cells. For the snow/ice cover, we used simulations from the Canadian Center for Climate Modelling and Analysis (CCCM II; `www.cccma.bc.ec.gc.ca`). This Gaussian grid spacing is roughly $3.8° \times 3.8°$ in longitude and latitude. The model gives the monthly mean snow/ice cover for each

grid cell. The simulations of the earth's albedo were performed using two different cloud cover data sets.

Our primary dataset for the model calculations is uncalibrated images of the global cloud cover produced by the Weather Services International (WSI) Corporation. We use these data in the simulations of our observations. The WSI Corporation is the only place we know of that is currently producing near real-time, on-line publication of global cloud cover maps. WSI maps (`www.intellicast.com`) are composed of data from both geostationary and polar orbiting satellites, including: GOES7, GOES8, METEOSTAT 5 and POES. Data from multiple orbits are mosaicked together to provide wide-scale global and full earth views in a single image. To allow for continuous night and day viewing of cloud patterns, infrared imagery is used. We download and calibrate daily WSI images.

For studies in Paper III, covering longer period of time, we will use the D2 revised algorithm (Rossow, 1996) monthly and daily mean fractional cloud cover data from International Satellite Cloud Climatology Project (ISCCP). All results reported in this paper however, derive from WSI daily data. The reason is that the WSI data are available, up-to-date and overlap with our observations.

The presently released ISCCP dataset covers 18 years over the period July 1983 through September 2001. We have used these calibrated data on a square grid, which is $2.5° \times 2.5°$ degrees in latitude and longitude. The ISCCP dataset makes use of visible and infrared radiances; total cloudiness is determined using both of them, whereas the various cloud types are determined using infrared radiances only. It has a spatial resolution of 280 km^2 cells, and the cloud fraction in each of them is determined by dividing the number of cloudy pixels by the total number of pixels per cell. Data are collected from a suite of weather satellites (including NOAA, METEOSAT, GOES-EAST, GOES-WEST, GMS satellites) operated by several nations and processed by several groups. All ISCCP data products are archived at the ISCCP Central Archive (`isccp.giss.nasa.gov`).

Whereas ISCCP cloud data is given in percentage cloud coverage, the WSI images we download from the web are given in arbitrary units, and it is necessary to translate them into fractional coverage. The daily WSI images are each placed on a "T42" square grid ($2.8° \times 2.8°$), as are the ISCCP data. We make use of the "T42" square grid because this is the format for snow and ice data, albeit one of the most common formats for climatological data. We have made WSI monthly mean cloud cover maps (values are in arbitrary units), and compared them with the ISCCP monthly mean maps (in units of fractional cloud cover). Primarily, we are looking for completely overcast areas. We find those areas with the minimum number of counts in the WSI images, and assign 100% cloud cover for any number of counts equal or greater to this mimima. We also look for clear sky scenes and we assign a maximum number of counts in WSI images below which we consider them to be 0% cloud cover. The values between the maxima and minima are converted to percentage coverage units using a simple polynomial parametrization. This yields an empirical non-linear calibration curve between the two cloud datasets, by which WSI daily maps in arbitrary units are converted into ISCCP fractional coverage, although this does not translate into a one-to-one correspondence between the two datasets. As we will see in Paper III, important differences between the two still occur. The use of a different calibration curve can altogether increase or decrease the mean albedo, but cannot increase the muted seasonal variations derived from the models. We emphasize that there is *no* inter-calibration between the model reflectances and those determined from our earthshine observations.

3. Comparing Daily Observations and Model Results

In Figure 1, we show evening and morning earthshine observations overlaid on model calculations covering the entire day. The two lower panels show the earthshine as a function of time (note that the time is plotted in reverse chronological order). The solid curve shows the variation of the calculated effective albedo A^* during the twenty-four hour period, and the solid boxes are the observed effective albedo. These results come from near to a quarter moon, and are compared with the earthwide WSI cloud cover from the same day in the top panel.

The top panel shows the cloud cover maps illustrating which parts of the earth contributes to the earthshine. We highlight (the large bright areas) those parts of the earth that are the source of the earthshine (i.e., are simultaneously in the sunshine and are visible from the moon at some time during the observations). The cloud cover is also shown as secondary grayscale, for instance, the east-west dark bands just north and south of the equator illustrate cloudless areas. We also indicate with boxes an intersection of the earth's surface with the bisectrix of the spatial angle between the surface intersection of the lines from the center of the earth to the moon and the sun or, in other words, the point of equal angles, where the angle of incidence is equal to the angle of reflection.

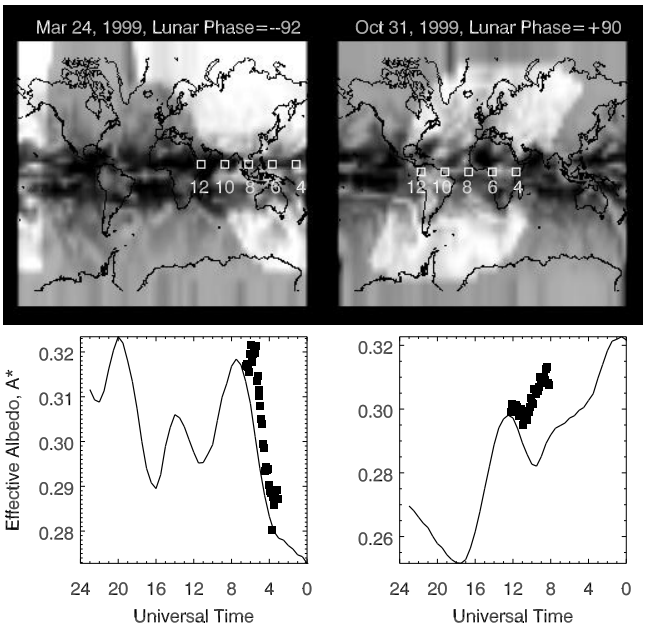

Figure 1. In the top panels, the extended bright areas highlight those parts of the earth that are the source of the earthshine. The satellite-derived WSI cloud cover maps are shown in a secondary gray-scale with brighter areas indicating greater cloud cover. For 31 October 1999, note that the northernmost regions are not sunlit, and the southernmost regions do not contribute to earthshine because the moon is fairly far north in the sky. The empty white boxes in the top panels indicate the longitudes of maximal contribution to the earthshine at the Universal Time (UT) shown. The solid boxes in the lower panels show the observed effective albedo as a function of time (note that the time axis is reversed), while the solid line indicates the simulated A^*.

The observations are consistent with the simulations for 24 March 1999, which is one of the nights for which the agreement is quite good. On 31 October 1999, a more typical night, there is a discrepancy of about 5% relative (or 0.015 absolute) in the effective albedo. One may notice offsets between the simulations and observations in the lower panels, but must bear in mind that the cloud cover data are a composite of many observations that are taken over about six hours (and sometimes up to 24). Thus, a precise timing between the observations and simulations is not possible. We simply assume that the cloud cover is invariant from one posting to the next and we make no effort to smooth the transition. If there were a rapid cloud formation or movement, it could result in observational and simulated results which do not have the same form. However, this does not account for the apparent offset in the albedo.

At high geographical latitudes above 45°, the cloud cover is fairly steady. Thus, the short timescale variations in reflectance in Figure 1 are due primarily to irregularities in the fractional cloud cover at low latitudes, and secondarily to the scene type. In the lower left panel of Figure 1, one sees that the observed and calculated maxima in A^* at 7:00 UT are due to a relative cloud excess over the Far East, while the calculated local minimum in A^* at 11:00 UT arises from the cloudless area above India and the Arabian Sea. In the lower left panel, there is a more than a 10% change in A^* over about two hours. This sharp increase is due to the increasing contribution of a cloudy Asia to the earth's reflectance as the earth rotates. An offset between the observed and calculated effective albedos is evident in the lower right panel. Typically, the observed results vary more about the mean than do the simulated ones. The larger variation in the observed results arises because the predicted seasonal variations are more muted.

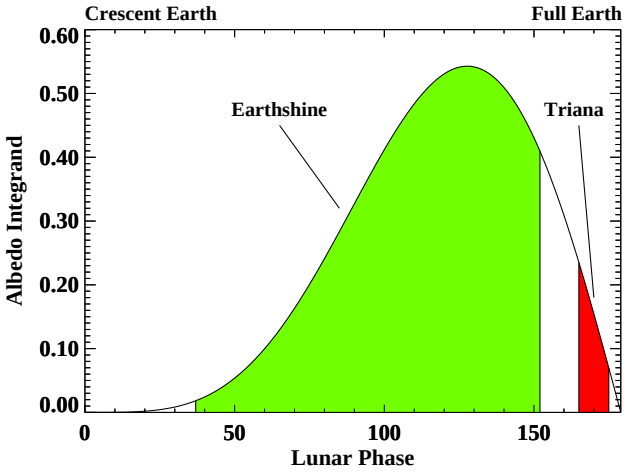

Figure 2. The kernel ($f_L(\theta)\sin\theta$) from which the Bond albedo is determined (see Equation 1) is shown as a function of lunar phase. Its behavior is dominated by the Lambert phase function for small phase angles, and by $\sin\theta$ for large phase angles. In green, we indicate contribution to the Bond albedo that arises from the range of lunar phases over which we measure the earthshine. In red, we show the approximate contribution from a satellite orbiting about L1, assuming the proposed orbit of Triana. If the orbit were to make larger loops around L1, as proposed by Lockwood (2002), all phase angles above 140° could be covered.

4. The Earth's Bond Albedo

To determine the Bond albedo, A, from our earthshine observations we need to integrate $A^*(\theta)$ over all phases of the moon using Equation (1). The kernel of the integrand, $f_L(\theta)\sin\theta$, is plotted in Figure 2. The figure illustrates one of the two basic problems in using the earthshine to determine the earth's Bond albedo. The first, and more significant problem, is that we cannot measure the earthshine for all phases of the moon. However, it is clear from Figure 2 that this becomes a problem for determining A predominately for lunar phases near the new moon, where the earth is most nearly Lambertian. Further, it can be seen in Figure 2 that the integrand in Equation (1) peaks near the quarter moon ($|\theta| \sim 130°$), when the moon shows a relatively sizable earthshine, while its phase is not so large that the earthshine is visible only briefly near sunset or sunrise. More precisely, to evaluate Equation (1) to an accuracy of 0.002 requires data for $|\theta| \geq 30°$. Thus, earthshine observations for most lunar phases are needed for an absolute value of the albedo, while observations near the full moon are most sensitive to variations in the albedo because so little of the earth is visible. The second basic problem in using the earthshine to determine the albedo arises because the orbit of the moon traces out an ellipse in the full three dimension space surrounding the earth, so we cannot measure the earthshine in all directions. Therefore, we are insensitive to any azimuthal anisotropy in the earthshine. Later in this section, we use simulations to show that the effect of the anisotropy is not significant, but it is systematic and one can account for it. We do this by taking advantage of full spatial coverage provided by the simulations.

4.1. Determining A from A^*

We have a two-step approach to determining the Bond albedo from the earthshine effective albedos. The first step

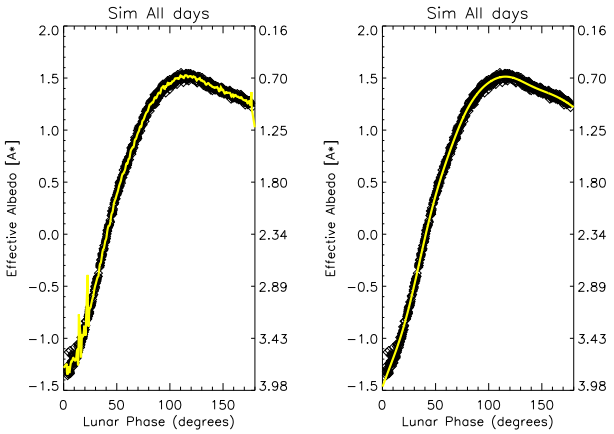

Figure 3. Each simulated, single night whole earth effective albedo is represented by an empty box. Since there are 898 nights, individual boxes cannot be resolved. The nights span the period from December 1998 to March 2002, and are the nights for which we have cloud cover data. Left panel: A least-squares fit to the data is shown, with the effective albedo being determined in individual bins that are 1° wide. Note the short wavelength oscillations for all phase angles. Right panel: The regularized fit to the same data. On the right hand y-axis, we use units of A^*.

is utilizing the simulations. Simulations for the three years of data for all nights that we have cloud cover are shown in both panels of Figure 3 (including all phase angles). The left and right panels show the same data. In the left panel, we show a least-squares fit in which the effective albedo is determined for 180 bins of 1° apiece. The least-squares fit is made using

$$\chi^2 = \frac{1}{(N - N_f)} \sum_{j=1}^{N} \left(\frac{\Delta A_j^*}{\sigma_j} \right)^2, \qquad (7)$$

where N and N_f are the number of nights simulated and the number of degrees of freedom in the solution, and where ΔA_j^* and σ_j are the deviation of A_j^* from the fit and the error in the determination of A_j^*, respectively. There are short wavelength oscillations in $[A^*]$, which are largest at the extreme phase angles. The extreme phase angles do not contribute to the Bond albedo, which is 0.2939±0.0001 for the least-squares fit. The short wavelength oscillations are an unpleasant artifact of the least-squares method. We could, instead, perform a least-squares fit with a low degree polynomial, which would suppress the oscillations. However, the meaning of the stiffening would be unclear. We believe that the effective albedo should be a smoothly varying function, and we impose this in a mathematically meaningful way – regularization – in which we minimize

$$\chi^2 (1 - \frac{N}{N_f}) + \lambda \int_{-\pi}^{\pi} [\theta^2 \frac{d^2}{d\theta^2} (\frac{\Delta A_j^*}{A^*})]^2 d\theta, \qquad (8)$$

where ΔA_j^* is the difference between the j^{th} data point and the fit to the data (the quantity we are determining) in the right panel of Figure 4, while λ is the regularization parameter which is, in reality, a smoothing constraint. In principle, the parameter is adjusted until χ^2 per degree of freedom is unity, so that the errors in the data are converted to comparable errors in the fit. However, the χ^2 space is relatively flat, so one typically weakens λ until short wavelength oscillations almost begin to appear in the fitted A^* function. Other forms of the constraint are certainly possible, but a second derivative constraint seems to work best here. In applying the regularization to the right panel, we have the advantage of being able to directly compare the obtained value of 0.2937± 0.0003 to that obtained by simple least-squares (0.2939±0.0001). The two results are consistent, and known with about an order of magnitude greater precision than we have been discussing for the observations. The error in the Bond albedo from regularization is about three times greater than that from the least-squares determination. This is due to the unphysical variation introduced by the short wavelenght variation. Still, the regularization introduces a point-to-point correlation in the errors, but we shall see that this effect is small, and the errors very nearly take the standard meanings.

Note that in Figure 3 we have observations for all lunar phase angles, averaged over the whole day, which give us a large number of points and a small spread of the modelled values, as our models are overly smooth. Hence our determination of the albedos with such small error on the integration. Those errors do not correspond to our measurement precision for the albedo from observations, which is an order of magnitude lower.

Next, we apply regularization to the subset of nights shown in the left panel of Figure 4, and using essentially the same regularization parameter as in Figure 3, and after assuming the left panel and right panel have the same values at phase angles of 0 and 180°. The left panel is the subset of 24-hour simulations for which we have observational data taken on the same calendar day. The resulting fit is shown in both the left and right panels of Figure 4. It can be seen that the fit to the subset of the data fits the whole of the data quite well, especially for the range of phase angles that is so important in determining the Bond albedo. With this fit, we find a Bond albedo of 0.298±0.001, which we regard as being consistent with the pure least-squares and regularization results of Figure 3, after recognizing the fact that 2/3 of the nights in the right panel of Figure 4 are absent in the left panel. The fit is fairly insensitive to the choice of λ over nearly an order of magnitude. For a review of regularization and its utility, see Goode (1995).

The second step in determining the Bond albedo for the observations is a further effort to account for the fact that the observational data do not span all phase angles. For this, we next examine the A^* simulations for the daytime region of the earth visible from the moon, for phase angles between 60 and 120° – the regime for which we have the most confidence in the data. In Figure 5, we show a scatter plot of the Bond albedo for a twelve month running mean vs. the contribution to that integral coming from phase angles between 60 and 120°. To construct the 12-month running mean, we start from the period December 1998 to November 1999 and then remove the first month and add a new one until the period April 2001-March 2002. The correlation between the total and "partial" integration values is 0.98. To test this method we have repeated it using the interval 90-120 degrees, and we get a correlation between total and

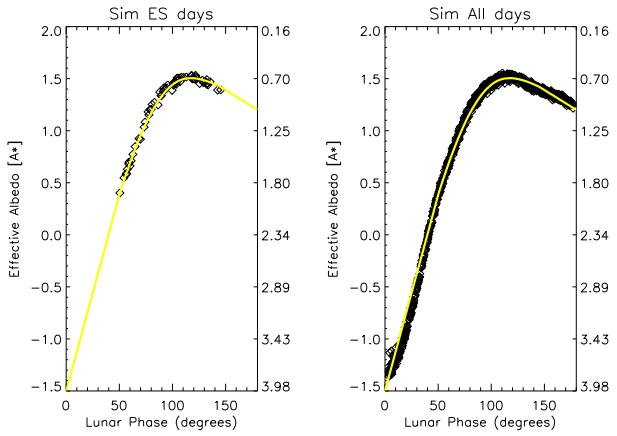

Figure 4. Each box represents a whole earth (i.e., covering a twenty-four hour period) simulated albedo. Left panel: Whole earth simulations for which the twenty-four hour period includes nights for which we have earthshine data and cloud cover (268 nights). The 268 nights span the period from December 1998 to March 2002. Right panel: Whole earth simulations for all twenty-four hour periods, during the same period, for which we have cloud cover data (898 nights – 466 during the waxing moon and 432 during the waning phase). The yellow curve in both panels is derived from the constrained or regularized least-squares fit to the left panel. On the right hand y-axis, we use units of A^*.

"partial" integration of 0.99. The linear fit gives us a way of converting a partial integral to a total integral. The albedos obtained by converting the partial integrals and from the total integrals are practically indistinguishable. After experimentation, we find that this approach returns more reliable values for the albedo than a simple regularization fit as used here in the left panel of Figure 4 and in Goode et al. (2001).

We next use this linear relation to determine a Bond albedo from the observational data. Again, we use the daytime earth's region visible from the moon simulation points at 0 and 180° to fix the regularization, and then determine the Bond albedo by scaling the fit between 60 and 120° by the same linear factor as used in determining the Bond albedo for the simulations at all available lunar phases. Applying the same regularization to the observational data of Figure 10 (see next section), which contains as a subset the 268 nights in the left panel of Figure 4, over a 3+ year period we find the mean Bond albedo for the earth to be 0.295±0.002 (0.293±0.003 for the evening observations and 0.296±0.002 for the morning). The deviations will contain not only the noise, but also any seasonal and long-term albedo variability that might have occurred during this period. The fit is shown in the the left panel of Figure 7. The right panel shows the corresponding fit for the simulations covering the same times and parts of the earth that contribute to the earthshine, for which we calculate an albedo of 0.298±0.001. The larger deviations in the observational results are indicative of the greater spread of the observational points about the mean (compare the left and right panels of Figure 7).

One of the prices paid for using regularization is that the point-to-point values of the solution are correlated, implying that the meaning of the errors is somewhat damaged. The damage is reflected in errors that are smaller than they are in reality. For instance, if the constraint were dominant, the uncertainty at each point in the solution would be the standard deviation of the mean. To ascertain whether the uncertainties quoted in this section are significantly too small, we also determined the errors in a completely different way, which does not suffer from the limitations imposed by regularization, and reveals that they are not significantly too small (section 4.4).

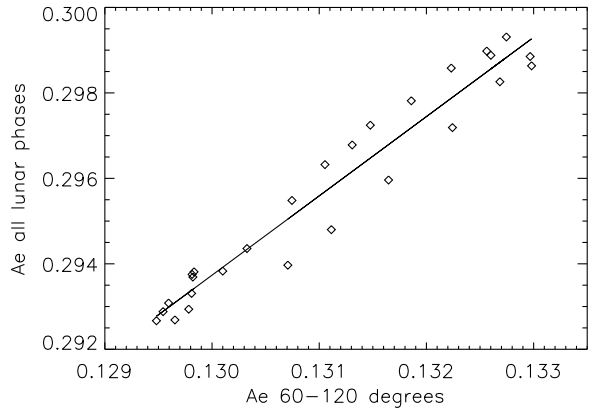

Figure 5. Scatter plot of the mean bond albedo for whole earth simulations, integrated over all lunar phases angles, and the integration value over lunar phase angles from 60° to 120° only. Each point is a 12-month mean, starting with the period December 1998-November 1999 for the first point, January-December 1999 for the second, and so on until April 2001-March 2002 for the last point. The correlation coefficient between these two integrations is 0.98.

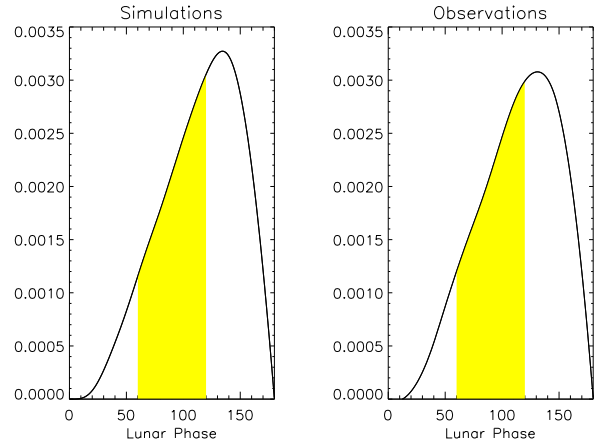

Figure 6. Left: The integrand of Equation (1) (kernel of Figure 2 multiplied by $A^*(\theta)$) using the 3+ years 24-hour simulations at all phases. Right: The same integrand using 3+ years of observational data. The area between 60 and 120 degrees is shaded in both figures.

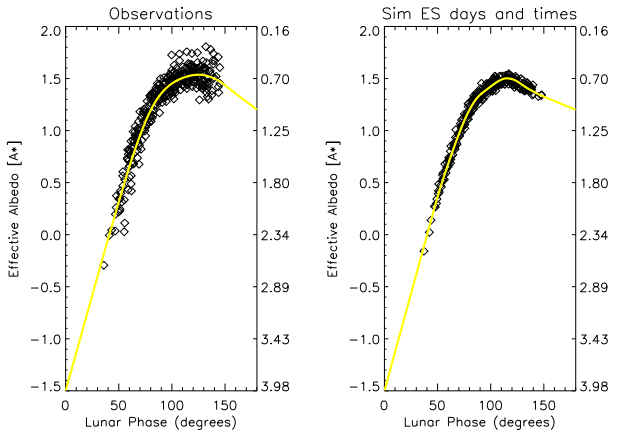

Figure 7. Observed (left panel) $[A^*]$'s plotted against the absolute value of the lunar phase from 225 clear observing nights from December 1998 through March 2002. Simulations (right panel) are shown covering the time intervals and parts of the earth that contribute to the earthshine signal for the 268 nights for which there were observations and contemporaneous cloud cover data. Each data point represents a nightly average of a series of 0.5-3.0 minute earthshine measurements taken once every five minutes with 0.1-5.0 second moonshine observations interspersed. Error bars for each night would be within the symbols. For the 268 nights for which we have observations and simulations, constrained least-square fits to the data and simulations are shown by the yellow curves. On the right y-axis, we use units of A^*.

4.2. Effect of Anisotropy

As mentioned at the beginning of this section, one concern about measuring the earthshine to precisely determine the earth's albedo is the amount of anisotropy in the earth's scattering. At any instant, the moon subtends $0^{\circ}.5$ as seen from the earth, and the obliquity of the moon's orbit extends this coverage over the lunar month to only 6° on either side of the ecliptic; thus, earthshine is not sensitive to light scattered out of the ecliptic. We can directly test the sensitivity by comparing the result of simulating the Bond albedo for the *whole* earth to that using the simulated earthshine. For the case of the earth that is in the sunshine, we use Equation (4) and calculate an average for the more than three years of data, A=0.3001±0.0002. For the whole of the earth in the earthshine, we are effectively assuming that for all lunar phases the earthshine does not depend on the azimuthal scattering angle. We test Equation (1) by using $A^*(\theta)$ from the least-squares fit in the left panel of Figure 3, from which we determined an equivalent 3+ year average Bond albedo of 0.2939±0.0001. The discrepancy arises because the relatively brighter polar regions are sometimes in the sunshine, but not in the earthshine. For this reason the bond albedo values obtained from our earthshine observations and our A* simulations should be increased by 0.006. This effect is illustrated in the right panel of Figure 1 for which the moon is northerly in the sky and doesn't receive light from the sunlit southernmost regions of the earth.

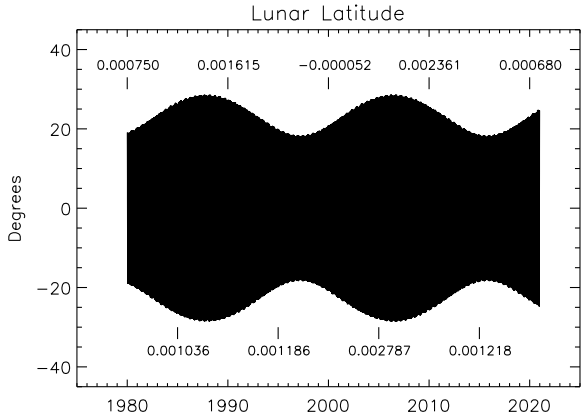

Figure 8. The precession of the moon's orbital plane with a period of 18.6 years induces a corresponding periodicity in the earth's albedo. The figure shows simulations for the period 1980-2020, using 25th January 1999 cloud cover data as though all nights were "frozen" in time with the same cloud cover. Also indicated, for some of the years, are the mean annual changes in Bond albedo, with respect to the albedo for 1999, caused solely by the evolving lunar declination. The albedo was simulated using Equation (1). During any small time interval, the position of the moon changes, but within the limits defined by the envelopes to the plot. Thus, the monthly changes give rise to the smeared appearance within the envelope.

Table 1. Effects of the nutation of the moon's orbital plane comparing similar times (left) and different epochs (right)

Span of Years	A_e	$\Delta A_e/A_e$ in %
1996(jan) - 1998(mar)	0.29453	$[A_e(3) - A_e(1)]/A_e(1) = 1.1\%$
2002(jan) - 2004(mar)	0.29612	$[A_e(2) - A_e(1)]/A_e(1) = 0.7\%$
2008(jan) - 2010(mar)	0.29623	$[A_e(3) - A_e(2)]/A_e(2) = 0.3\%$

4.3. Precession of the Lunar Nodes

A higher order difficulty in determining the earth's reflectance from the albedo is that the intensity of the earthshine varies with the precession of the lunar nodes. That is, because the gravitational effects of the sun and moon are not always the same, there is some wobble in the motion of the earth's axis; this wobble, called nutation, causes the celestial poles to move, not in perfect circles, but in a series of S-shaped curves with a period of 18.6 years. This precession of the moon's orbital plane has a period of 18.6 years. The sensitivity of the earthshine arises from the anisotropy of the light scattered by the earth. For example, when the declination of the new moon is a maximum (some 29°), and it is near the northern-summer solstice, more of the arctic polar ice cap is visible and the earthshine will be brighter. Some nine years later, the lunar declination under the same conditions will be only 18°, and the earthshine will be at a minimum. We have performed simulations to study this effect and the results appear in Figure 8 and the Table 1. It is clear from the figure that the nutation of lunar nodes perturbs $[A^*]$ at the $0^m.004$ level (A^* at 0.0012 level) or less, or about five times smaller than the effect of anistropy. It is straightforward, but necessary to account for this in comparing earthshine results from different epochs.

4.4. Alternate Determination of Uncertainties in the Bond Albedo

In calculating the Bond albedo, we have an alternative way to connect the precision to which we determine the $[A^*]$ to the accuracy to which we determine A. To do this, we use the daily WSI cloud cover maps and calculate the whole earth albedo A, the effective earth's albedo $[A^*]$ and the variation of each during the full day and during the times for which we have earthshine observations. For the calculations, we use a third-order polynomial fit to $[A^*]$, which defines a mean calculated effective albedo for the earth, $\overline{[A^*(\theta)]}$,

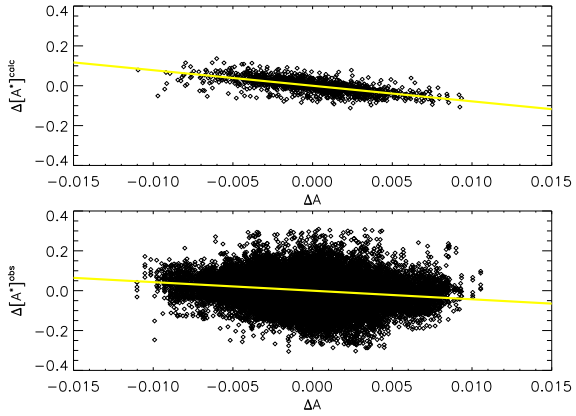

Figure 9. Top: Linear correlation of the calculated earthshine anomaly, $\Delta[\mathrm{A}^*]^{\mathrm{calc}}$, with the calculated global albedo anomaly, ΔA for 1694 calculations for lunar phase angles for which $140^{\circ} \geq |\theta| \geq 40^{\circ}$. Bottom: Linear fit to observational anomalies, $\Delta[\mathrm{A}^*]^{\mathrm{obs}}$, during the same time periods, assuming ΔA is the same as that from the calculations.

and residuals, $\Delta[A^*]^{calc} = [A^*] - \overline{[A^*(\theta)]}$; the latter carry information about the weather, climate and surface type. Their correlation with the calculated global albedo anomalies ($\Delta A = A - \overline{A}$) at the times at which earthshine observations have been taken, is shown in the top panel of Figure 9, where we have included the 268 nights for which we have simultaneous cloud cover data and earthshine observations.

For the observational data, we make a scatter plot during the same periods, and assume they correlate with ΔA, as shown in the lower panel of Figure 9. In detail, we used a third-order polynomial fit to define a mean observed effective albedo $\overline{[A^*(\theta)]}$ and observed residuals $\Delta[A^*]^{obs}$. Their correlation with the global calculated albedo anomalies ($\Delta A = A - \overline{A}$) is shown in the lower panel of Figure 9 including a linear fit to the points. This figure gives us insight into how accurately we can measure the albedo. The large number of points in the lower panel comes from the fact that in order to make a direct comparison, we interpolate our 30-minute resolution ΔA from simulations for each time at which an observation is taken (a period between 0.5-3.0 minutes). Whereas in the top panel, a direct comparison between ΔA and $\Delta[A*]^{calc}$ is done. The correlations are -0.66 and -0.27 in the top and lower panels respectively, both significant at higher than a 99.99% confidence level.

Using Figure 9, we note that a variation in A of 0.01 corresponds to changes in $[A^*]^{obs}$ of $0^m.043$ (or 4.0% in the observed A^*, using $\delta[A^*] = \frac{\ln 10}{-2.5}\frac{\delta A^*}{A^*} = -1.08\frac{\delta A^*}{A^*}$) and to a change in $[A^*]^{calc}$ of $0^m.078$ (or 7.2% change in the calculated A^*). Equivalently, a 1% earthshine measurement of A^* determines the albedo with a precision of 0.0025. To place this precision in context, we note that independent satellite determinations of the monthly mean albedo can differ by 0.005 or more, and that the seasonal range of the monthly mean albedo is 0.015 or more (see Figure 12). The individual simulated points have error bars of about 0.005 and the seasonal variations have an amplitude of 0.027.

Our nightly $\sim$ 2% observational uncertainty in each nights measurement of A^* corresponds to a deviation in of $\sim 0^m.02$ $[A^*]$, which implies measuring A to ± 0.005. This value is comparable to that from satellite data (Seiji et al, 2002). From the figure, we converted the error in $[A^*]$ into the error in A, which averaging over a year, implies measuring A to slightly better than 0.005 (or to about 0.003 over three years) – even though we have observed about a third of the nights in the year. These uncertainties are similar to those we determined using constrained least-squares for A. Thus, we conclude that the regularization has not underestimated the uncertainties in a meaningful way (Gibson et al, 1990).

5. Bond Albedo during 1999-2001

5.1. Observation Results 1999-2001

Figure 10 illustrates the change in $[A^*]$ against lunar phase angle as determined from the nightly earthshine observations – with the morning and evening observations presented separately, and combined. In the plots, each data point represents a nightly averaged $[A^*]$ value, with which we study the changes in $[A^*]$ for different nights, months and seasons. One may first note that while $[A^*]$ is relatively flat near the quarter moon, the flatness implies a near-Lambertian earth for most lunar phase angles (see Equation (9) of Paper I). However, with the moon approaching full phase and θ getting closer and closer to 180^o, the earth as seen from the moon, becomes a thinner and thinner crescent, and so earth-reflected radiation reaching the moon is more and more dominated by forward scattering in the atmosphere. For lunar phase angles much below about 40°, we presently regard the results as unreliable because of the proximity of the earthshine fiducial patches and the terminator (the transition from the moonshine to the earthshine is not sharp). Further, we do not have reliable earthshine data near the new moon (much beyond a lunar phase angle of about 140°) because the earthshine is visible for only a brief time near sunset or sunrise, depending on whether the moon is in its waxing or waning phase. Thus, the extrapolation to zero airmass is unreliable. For large lunar phase angles, it is also difficult to find a fiducial patch that is confined to the moonshine.

A detailed examination of Figure 10 reveals that, with respect to the fitted mean, the $[A^*]$ determined from the local Big Bear Solar Observatory (BBSO) morning observations (lunar phase angle > 0) are not apparently distinct from those determined from the local evening observations (lunar phase angle < 0); i.e., the earthshine data from BBSO nights implies that the contemporaneous sunlit parts of the earth are equally shiny in the evening and in the morning. Ultimately, we determine from the earthshine data a mean albedo of 0.293±0.003 for the evenings and of 0.296±0.002 for the mornings. The lack of a significant difference may

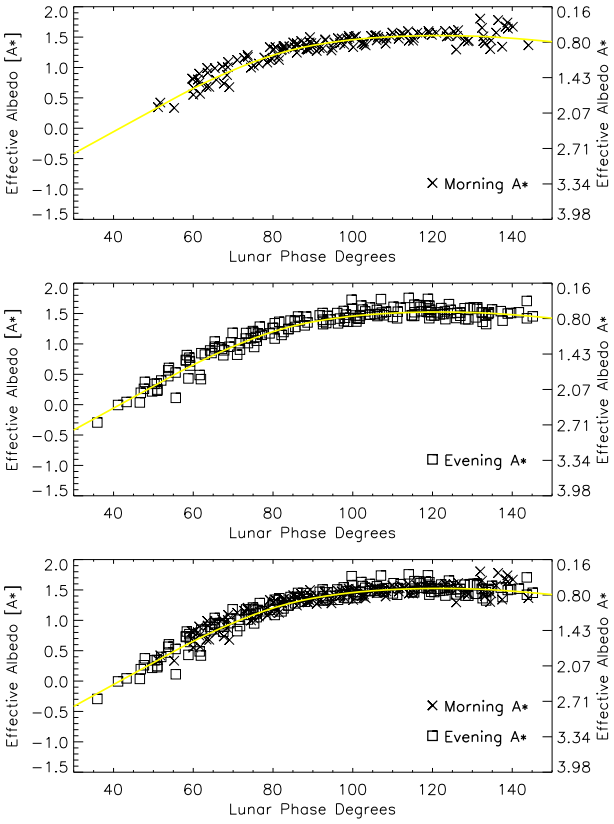

Figure 10. Plot of the mean $[A^*]$, which is determined from 25 sets for each night, for (top) morning and (middle) evening observations. The bottom panel gives the combined results for mornings and evenings. In the figure, 340 nights of observations are included (150 nights of morning observations and 190 evening). The solid line in all panels indicates the curve from the fit to the data in the bottom panel, as described in §6. On the right y-axis, we use units of A^*.

seem somewhat surprising because the earthshine we observe in the mornings and in the evenings comes from the reflection of sunlight from different parts of the earth. In our evening observations, the earthshine is dominated by southeast Asia. In the mornings, the earthshine is dominated by Africa, Europe and the Atlantic.

One might think that the agreement between evening and morning determinations results from fortuitous compensations from the afternoon/evening development of deep convection versus morning maxima of low stratified clouds. But most likely, the agreement is due to the large area-average in our earthshine Bond albedo integrations, which contains a wide mix of different land, ocean, ice and cloudy areas.

Bearing in mind that a change in $[A^*]$ of $0^m.01$ corresponds to about a 1% change in A^*, we observe a roughly $\pm 5\%$ night-to-night variation in the effective albedo, A^*, even near the quarter moon where the data are most reliable. This variation is primarily associated with night-to-night changes in the cloud cover, rather than some error in the data collection/reduction process. In Figure 10, the spread about the mean is even larger, and we shall see that this is primarily associated with seasonal and long-term variations in the reflectance (Paper III; Goode et al., 2001).

To better understand the influence of the earth's varying topography and cloud cover on $[A^*]$, we plot the albedo as observed throughout single nights in Figure 11. This plot comes from using Equation (2) after each point is corrected for airmass, and inputting the proper lunar phase for each observed timepoint. Note that the lunar phase function changes by about 0.5° per hour. In Figure 10, each point represents the mean of a single night. In each panel of Figure 11, the mean for the night is given as a number. In Figure 11a and Figure 11b, observations of two nights with almost the same lunar phase, but from different months, are compared. Both observations were made in the evening at BBSO (as opposed to the early morning). They demonstrate a common tendency of an early decrease in $[A^*]$, or a brightening earth, as the sun is rising over Asia, increasing the contribution from the relatively bright Asia, although the trend is more apparent in Figure 11a. The sun rising over a cloudy Asia causes a 5-10% change in A^* over the period of the observations. Even though the temporal evolution of the points in Figures 11a and 11b closely resemble each other, the mean value of A^* in Figure 11a is 5% smaller. This difference reflects a greater Asian cloud cover on March 24 than July 20. As we shall see in Paper III, some part of the appreciable difference is probably due to seasonal changes in cloud cover, rather than differences in the part of the world we are measuring. In Figures 11c and Figure 11d, the observations are from two mornings at similar phases of the moon, and covering comparable local times. One notices immediately, that the A^* in Figures 11c and 11d are about 10% smaller that their counterparts in 11a. In Figures 11c and 11d, each panel shows an increasing $[A^*]$, or a darker earth, as time goes on. This is because the sunrise over the Atlantic is increasing the role of the darker, and less cloudy, ocean in the earthshine.

As shown in Paper I for one night, if we combine nights to obtain, say, a yearly average, then the total deviation, from all sources of uncertainty, will be smaller, but no smaller than that associated with the mean values of the various lunar phase functions and the ratio of the geometrical albedos. For instance, we have 340 nights of data for which the fit to Beer's Law has a standard deviation of less than 1% for the single pair of fiducial patches used by Goode et al. (2001). We regard these as our "good" nights. If we calculate the standard deviation of the mean for the 150 (190) mornings (evenings) pairs, we find 0.8% (0.7%). Combining this with the uncertainty in the lunar phase, we find a deviation of less than 1% in the binned A^*'s. Such error bars would be well within the symbols of Figure 10. The most likely source of systematic errors is the determination of the geometrical albedos, coming from a single lunar eclipse, but such systematic errors would not change the spread in the points. If the presumed systematic errors were comparable to the measurement errors we can reasonably identify, they are still considerably smaller than the spread in the $[A^*]$'s that appear in, say, Figure 10.

5.2. Model Results 1999-2002

In Figure 12, we show daily mean global albedos from our simulations of the whole earth covering 1999.0-2002.3, and calculated using Equation (4) and WSI daily cloud maps. Roughly, the figure shows peaks in the earth's reflectivity in the fall and spring, while showing minima in the winter and summer. From this, we determine a mean Bond albedo of 0.3 over that period. We note that the size of the spread in night-to-night variations is comparable to the amplitude of the seasonal variability.

Applying Equation (6), we also simulated the observed effective albedo shown in Figure 10 covering *the same parts of the earth at the same time*. The results are shown in Figure 13. Note that the distribution is tighter to the fit than in Figure 10. Thus, the greater scatter in Figure 10 cannot be due to different nights for the same lunar phase seeing different parts of the earth, because each night's simulation covers exactly the parts of the earth which are observed. However, like the observational results, there is no clear distinction between the simulations for morning and evening. As in Figure 10, it is also clear from the simulations shown in Figure 13 that the evening data have a greater scatter about the mean than do the morning data. This implies a more variable cloud cover over Asia. In Figure 14, we show

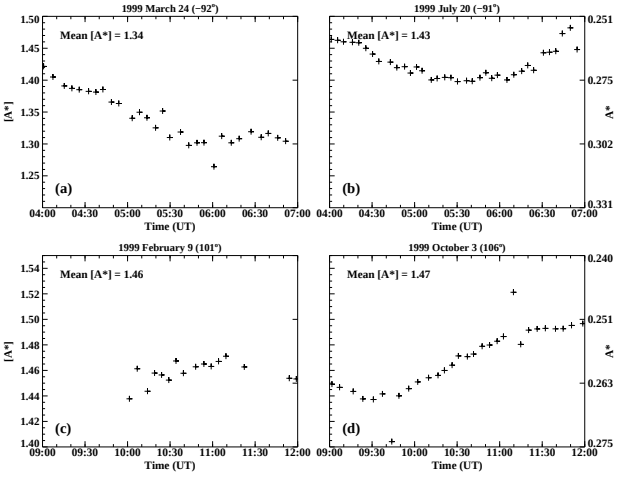

Figure 11. Plots of $[A^*]$ observed in the night of (a) 1999 March 24, (b) 1999 July 20, (c) 1999 February 9, and (d) 1999 October 3, against the time of observations. The right y-axis gives the result in units of A*. The values are derived for the fiducial pair used in Goode et al. (2001) and as indicated in Figure 3

the same kind of plot as Figure 13, but covering the entire earth for nights for which we have observations and cloud cover data (see the difference in coverage between the solid lines and solid boxes in Figure 1). Since the whole earth simulations average more of the globe, it is not a surprise that these simulations show considerably less scatter than those of a part of the earth. We also note that the mean effective albedo in our simulations, is higher for the whole earth than it is for the part we see by 0.016 ± 0.017 (1.3%) in A^*, i.e. the albedo increases when we add the third of the earth invisible to Big Bear. That may be a consequence of including the american land mass, although the result is not statistically significant.

We next consider how the results could change with a quite different lunar phase function, like that of Danjon.

5.3. Comparisons with Danjon's Results

To compare our results with those of Danjon, we show our data in Figure 15, but analyzed using Danjon's phase function (as shown in Figure 14 of Paper I). In Figure 15, the solid line shown is the fit from Figure 10, which is for the same nights, but analyzed with the correct phase function.

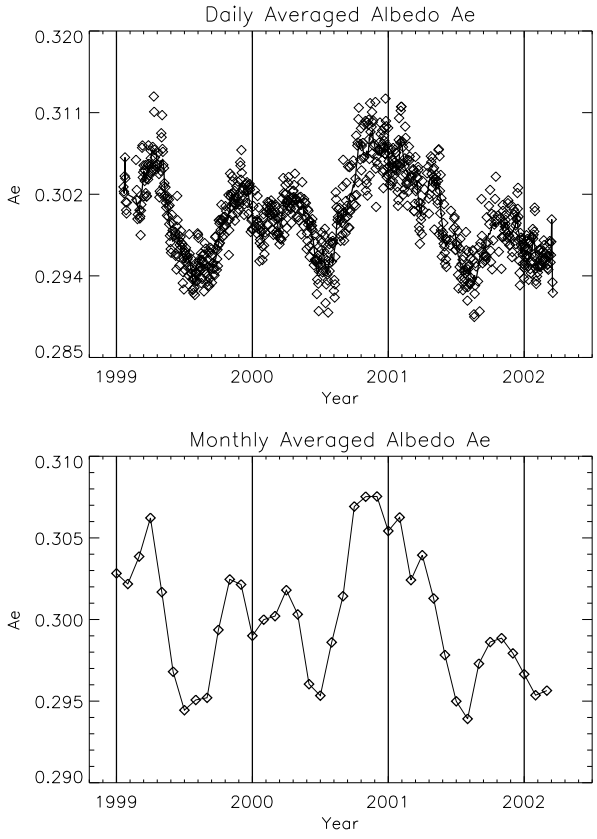

Figure 12. Top: Daily mean global albedos (diamonds) from the simulations beginning from January 1999 to March 2002. The albedo is calculated from snow and ice data from the Canadian Center for Climate Modeling simulations and WSI cloud satellite data, and includes the 24-hour albedo from all sunlit parts of the earth, whether visible from the moon or not. The bold solid line shows the 30-day running mean. The amplitude of the simulated seasonal variation of the whole earth albedo is 4-5%. Bottom: as in top panel, but daily means are averaged into monthly means.

Clearly, for phase angles below 100° the data tend to lie above the fit, while for phase angles above 100° the points tend to lie below the fit. To understand why Danjon found a Bond albedo about 0.1 larger than the true value, one must also inspect the kernel from which the Bond albedo is determined, see Figure 2, where the kernel peaks at about 130° (near the quarter moon). These phases are most significant in the determination of the albedo. Thus, the inconsistency between Danjon's albedo of about 0.40 and our observed

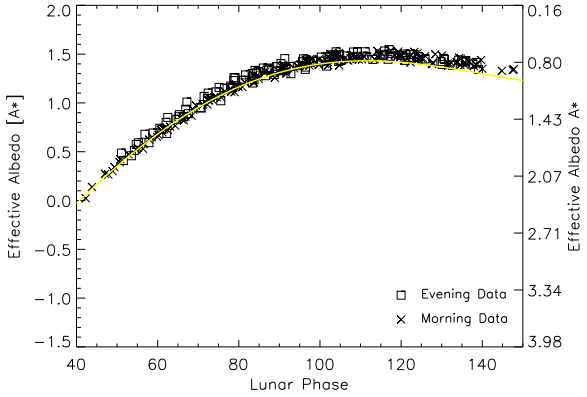

Figure 13. Plot of [A*] vs. absolute value of the lunar phase from simulations covering the same phases of the earth as the observational results in Figure 10; i.e., the simulations are looking at the regions of the earth visible from the moon at the times of our earthshine observations. Each data point represents the averaged [A*] value throughout one night; an "x" indicates morning observation (lunar phase > 0) and a "square" indicates evening observation (lunar phase < 0). For reference, the solid curve shown is fit to the data in Figure 10.

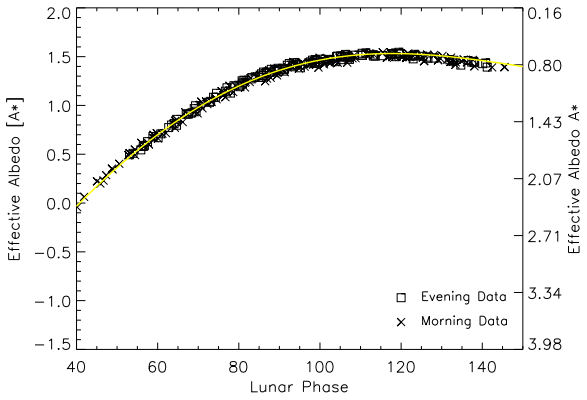

Figure 14. Plot of [A*] vs. absolute value of the lunar phase from simulations covering the whole earth for all days for which we have observations. Each point represents the 24-hour average of UT defined days for which we have earthshine data. The "x"'s and "squares"'s are given to show whether the 24-hour average is connected to observations at positive or negative lunar phase. For reference, the solid curve is the fit to the data shown in Figure 10.

value of 0.30 comes mainly from Danjon's underestimate of the lunar opposition effect (Flatte et al., 1991; MacDonald and Koonin, 1992), which carries over into the significant overestimate of the lunar phase function near the quarter moon that dominates the determination of the albedo.

6. Conclusions

From BBSO, we have observed the earthshine for more than three years. We determined a large scale average of the earth's albedo for major areas of the earth, including Europe, Africa and the Atlantic Ocean in our morning observations, when the sun is high over Africa and the Atlantic Ocean, and the moon is in its declining phase. We also measured the albedo for large areas in southeast Asia and the Pacific in our evening observations during the rising phase of the moon. From the earthshine data, we see that southeast Asia and West Africa/Southern Europe have very nearly the same albedo.

We have learned that the albedo we determine is as precise as determined from satellites, while providing an excellent complement. One of the obvious advantages of earthshine observations is having an absolute calibration coming from the bright side of the moon.

We have compared our results with models of the earth's scenes inputting contemporaneous snow/ice cover from models and cloud cover from satellites. We find a general agreement between the observed and modelled results, with the model results uniformly showing milder amplitude variations. This greater spread of the observations, such as seen in Figure 10, does not result from errors in our observations, but rather from seasonal and long-term changes in reflectance that are not captured by our models. Paper III of this series deals with these two aspects of the earth's reflectance variations. In sum, we conclude that our models, using daily mean cloud cover and a simplified model of the cloud radiative properties, are overly smoothed.

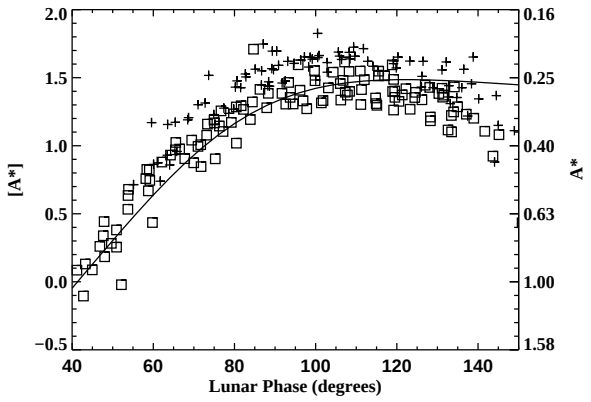

Figure 15. Danjon's lunar phase function (see Figure 14 in Paper I) was used to analyze our observational data. The solid curve is the regularized fit to the same data analyzed using *our* lunar phase functions, as in Figure 10. The points shown in this figure are those derived using Danjon's phase function. Since Danjon's phase function is systematically lower than the correct one for phase angles that make the largest contribution to A, this explains how Danjon derived an albedo of about 0.4 from his observations, which is much higher than our observed and simulated values of about 0.3.

Acknowledgments. This research was supported in part by a grant from NASA (NAG5-11007).

References

Danjon, A., Recherches sur la photométrie de la lumière cendrée et l'albedo de la terre, *Ann. Obs. Strasbourg*, 2, 165-180, 1928.

Danjon, A., Albedo, color, and polarization of the earth, *The Earth as a Planet*, ed. Kuiper, Chicago, 726-738, 1954.

Dubois, J., Le photomètre à ceil-de-chat et ses applicatons, *Ciel et Terre*, 58, 350-361, 1942.

Dubois, J., Sur l'albedo de la terre, *Bull. Astron.*, 13, 193-196, 1947.

Flatte, S., S.E. Koonin., and G. MacDonald, *Global Change and the Dark of the Moon*, JSR-91-315 (McLean, VA: The MITRE Corporation), 1991.

Gibson, G. G., F.M. Denn, D.W. Young, E.F. Harrison, P. Minnis, B.R. Barkstrom, O.C. Smith, D.J. Travers, Characteristics of the earth's radiation budget derived from the first year of data from the Earth Radiation Budget Experiment, *SPIE*, 1299, 253-256, 1990.

Goode, P.R., Internal rotation and structure of the sun, *ESA SP-376*, 121-136, 1995.

Goode, P.R., J. Qiu, V. Yurchyshyn, J. Hickey, M.C. Chu, E. Kolbe, C.T. Brown, and S.E. Koonin, Earthshine observations of the earth's reflectance, *Geophys. Res. Lett.*, 28 (9), 1671-1674, 2001.

Intergovermental Panel on Climate Change (IPCC), Climate Change 1992, Suppl. Rep IPCC Sci. Assess, ed. J.T. Houghton, B.A. Callender, S.K. Varney, Cambridge, MA: Cambridge University Press, 1992.

Intergovermental Panel on Climate Change (IPCC), Climate Change 1994, Radiative Forcing of Climate Change and an Evaluation of the IPCC 1992 Emission Scenarios, ed. J.T. Houghton, L.G. Meira Filho, J. Bruce, H. Lee, B.A. Callender, E. Haites, N. Harris, K. Maskell, Cambridge, MA: Cambridge University Press, 1995.

Lockwood, M., 2002, private communication.

Pallé, E., P.R. Goode, J. Qiu, V. Yurchyshyn, J. Hickey, P. Montañés Rodriguez, M.C. Chu, E. Kolbe, C.T. Brown, and S.E. Koonin, Earthshine and the earth's albedo III: Long-term variations in reflectance, *submitted*, 2003.

Qiu, J., E. Pallé, P.R. Goode, V. Yurchyshyn, J. Hickey, P. Montañés Rodriguez, M.C. Chu, E. Kolbe, C.T. Brown, and S.E. Koonin, Earthshine and the earth's albedo I: Precise and large-scale nightly measurements, *submitted*, 2003.

Rossow, W. B., A. W. Walker, D. E. Beuschel, and M. D. Roiter, International Satellite Cloud Climatology Project (ISCCP): Documentation of New Cloud Datasets, *WMO/TD-No. 737*, 115 pp, World Meteorological Organization, Geneva, 1996.

Seiji, K., N.G. Loeb, and C.K. Rutledge, Estimate of top-of-atmosphere albedo for a molecular atmosphere over ocean using Clouds and the Earth's Radiant Energy System measurements, *Journal of Geophysical Research*, 107 (D19), 4396, doi:10.1029/2001JD001309, 2002.

Suttles, J.T., R.N. Green, P. Minnis, G.L. Smith, W.G. Staylor, B.A. Wielicki, I.J. Walker, V.R. Young, and L.L. Stowe, Angular Radiation Models for Earth-Atmosphere Systems, *Vol. I: Shortwave Radiation, NASA Reference Publication RP-1184*, 26 pp, 1988.

Big Bear Solar Observatory, New Jersey Institute of Technology, Newark, NJ 07102, USA

(Received _____.)

Figure 1: In the top panels, the extended bright areas highlight those parts of the earth that are the source of the earthshine. The satellite-derived WSI cloud cover maps are shown in a secondary gray-scale with brighter areas indicating greater cloud cover. For 31 October 1999, note that the northernmost regions are not sunlit, and the southernmost regions do not contribute to earthshine because the moon is fairly far north in the sky. The empty white boxes in the top panels indicate the longitudes of maximal contribution to the earthshine at the Universal Time (UT) shown. The solid boxes in the lower panels show the observed effective albedo as a function of time (note that the time axis is reversed), while the solid line indicates the simulated A^*.

Figure 2: The kernel $(f_L(\theta)\sin\theta)$ from which the Bond albedo is determined (see Equation 1) is shown as a function of lunar phase. Its behavior is dominated by the Lambert phase function for small phase angles, and by $\sin\theta$ for large phase angles. In green, we indicate contribution to the Bond albedo that arises from the range of lunar phases over which we measure the earthshine. In red, we show the approximate contribution from a satellite orbiting about L1, assuming the proposed orbit of Triana. If the orbit were to make larger loops around L1, as proposed by Lockwood (2002), all phase angles above 140° could be covered.

Figure 3: Each simulated, single night whole earth effective albedo is represented by an empty box. Since there are 898 nights, individual boxes cannot be resolved. The nights span the period from December 1998 to March 2002, and are the nights for which we have cloud cover data. Left panel: A least-squares fit to the data is shown, with the effective albedo being determined in individual bins that are 1° wide. Note the short wavelength oscillations for all phase angles. Right panel: The regularized fit to the same data. On the right hand y-axis, we use units of A^*.

Figure 4: Each box represents a whole earth (i.e., covering a twenty-four hour period) simulated albedo. Left panel: Whole earth simulations for which the twenty-four hour period includes nights for which we have earthshine data and cloud cover (268 nights). The 268 nights span the period from December 1998 to March 2002. Right panel: Whole earth simulations for all twenty-four hour periods, during the same period, for which we have cloud cover data (898 nights – 466 during the waxing moon and 432 during the waning phase). The yellow curve in both panels is derived from the constrained or regularized least-squares fit to the left panel. On the right hand y-axis, we use units of A^*.

Figure 5: Scatter plot of the mean bond albedo for whole earth simulations, integrated over all lunar phases angles, and the integration value over lunar phase angles from 60° to 120° only. Each point is a 12-month mean, starting with the period December 1998-November 1999 for the first point, January-December 1999 for the second, and so on until April 2001-March 2002 for the last point. The correlation coefficient between these two integrations is 0.98.

Figure 6: Left: The integrand of Equation (1) (kernel of Figure 2 multiplied by $A^*(\theta)$) using the 3+ years 24-hour simulations at all phases. Right: The same integrand using 3+ years of observational data. The area between 60 and 120 degrees is shaded in both figures.

Figure 7: Observed (left panel) $[A^*]$'s plotted against the absolute value of the lunar phase from 225 clear observing nights from December 1998 through March 2002. Simulations (right panel) are shown covering the time intervals and parts of the earth that contribute to the earthshine signal for the 268 nights for which there were observations and contemporaneous cloud cover data. Each data point represents a nightly average of a series of 0.5-3.0 minute earthshine measurements taken once every five minutes with 0.1-5.0 second moonshine observations interspersed. Error bars for each night would be within the symbols. For the 268 nights for which we have observations and simulations, constrained least-square fits to the data and simulations are shown by the yellow curves. On the right y-axis, we use units of A^*.

Figure 8: The precession of the moon's orbital plane with a period of 18.6 years induces a corresponding periodicity in the earth's albedo. The figure shows simulations for the period 1980-2020, using 25th January 1999 cloud cover data as though all nights were "frozen" in time with the same cloud cover. Also indicated, for some of the years, are the mean annual changes in Bond albedo, with respect to the albedo for 1999, caused solely by the evolving lunar declination. The albedo was simulated using Equation (1). During any small time interval, the position of the moon changes, but within the limits defined by the envelopes to the plot. Thus, the monthly changes give rise to the smeared appearance within the envelope.

Figure 9: Top: Linear correlation of the calculated earthshine anomaly, $\Delta[\mathrm{A}^*]^{\mathrm{calc}}$, with the calculated global albedo anomaly, ΔA for 1694 calculations for lunar phase angles for which $140^\circ \geq |\theta| \geq 40^\circ$. Bottom: Linear fit to observational anomalies, $\Delta[\mathrm{A}^*]^{\mathrm{obs}}$, during the same time periods, assuming ΔA is the same as that from the calculations.

Figure 10: Plot of the mean $[A^*]$, which is determined from 25 sets for each night, for (top) morning and (middle) evening observations. The bottom panel gives the combined results for mornings and evenings. In the figure, 340 nights of observations are included (150 nights of morning observations and 190 evening). The solid line in all panels indicates the curve from the fit to the data in the bottom panel, as described in §6. On the right y-axis, we use units of A^*.

Figure 11: Plots of $[A^*]$ observed in the night of (a) 1999 March 24, (b) 1999 July 20, (c) 1999 February 9, and (d) 1999 October 3, against the time of observations. The right y-axis gives the result in units of A*. The values are derived for the fiducial pair used in Goode et al. (2001) and as indicated in Figure 3

Figure 12: Top: Daily mean global albedos (diamonds) from the simulations beginning from January 1999 to March 2002. The albedo is calculated from snow and ice data from the Canadian Center for Climate Modeling simulations and WSI cloud satellite data, and includes the 24-hour albedo from all sunlit parts of the earth, whether visible from the moon or not. The bold solid line shows the 30-day running mean. The amplitude of the simulated seasonal variation of the whole earth albedo is 4-5%. Bottom: as in top panel, but daily means are averaged into monthly means.

Figure 13: Plot of [A*] vs. absolute value of the lunar phase from simulations covering the same phases of the earth as the observational results in Figure 10; i.e., the simulations are looking at the regions of the earth visible from the moon at the times of our earthshine observations. Each data point represents the averaged [A*] value throughout one night; an "x" indicates morning observation (lunar phase > 0) and a "square" indicates evening observation (lunar phase < 0). For reference, the solid curve shown is fit to the data in Figure 10.

Figure 14: Plot of [A*] vs. absolute value of the lunar phase from simulations covering the whole earth for all days for which we have observations. Each point represents the 24-hour average of UT defined days for which we have earthshine data. The "x"'s and "squares"'s are given to show whether the 24-hour average is connected to observations at positive or negative lunar phase. For reference, the solid curve is the fit to the data shown in Figure 10.

Figure 15: Danjon's lunar phase function (see Figure 14 in Paper I) was used to analyze our observational data. The solid curve is the regularized fit to the same data analyzed using *our* lunar phase functions, as in Figure 10. The points shown in this figure are those derived using Danjon's phase function. Since Danjon's phase function is systematically lower than the correct one for phase angles that make the largest contribution to A, this explains how Danjon derived an albedo of about 0.4 from his observations, which is much higher than our observed and simulated values of about 0.3.